Ab-initio Band Structure Calculations and ^{61}Ni-Mössbauer Studies of $BaNiO_2$, $BaNiO_3$ and CaNiN *

B. Hannebauer[a], P. C. Schmidt[a], R. Kniep[b], N. Jansen[c], D. Walcher[c], P. Gütlich[c], R. Gottschall[d], R. Schöllhorn[d], and M. Methfessel[e]

[a] Inst. f. Physikal. Chemie, Techn. Hochschule Darmstadt
[b] Eduard-Zintl-Institut, Techn. Hochschule Darmstadt
[c] Inst. f. Anorg. Chemie und Analyt. Chemie, Johannes-Gutenberg-Universität Mainz
[d] Inst. f. Anorg. und Analyt. Chemie, Techn. Universität Berlin
[e] Inst. f. Halbleiterphysik, Frankfurt (Oder)

Z. Naturforsch. **51a,** 515–526 (1996); received December 27, 1995

The electron density distribution of the nickel compounds $BaNiO_2$, $BaNiO_3$ and CaNiN has been investigated experimentally by ^{61}Ni Mössbauer spectroscopy and theoretically by band structure calculations using the FP-LMTO (*F*ull *P*otential *L*inear *M*uffin-*T*in *O*rbital) method. For all compounds good agreement is found between the experimental and theoretical values of the electric field gradient $q^{\text{exp.}}$ and $q^{\text{theor.}}$ at the nickel site.

$BaNiO_2$ contains nickel in a square-planar coordination forming puckered chains of edge-sharing NiO_4 squares. $|q|$ at nickel is large: $q^{\text{exp.}} = -15.7\,(1.5) \cdot 10^{21}\ \text{Vm}^{-2}$ and $q^{\text{theor.}} = -15.59 \cdot 10^{21}\ \text{Vm}^{-2}$.

The principal axis z is perpendicular to the NiO_4 squares. The crystal structure of $BaNiO_3$ contains face-sharing chains of NiO_6 octahedra. In $BaNiO_3$ q(Ni) is small: $q^{\text{exp.}} = \pm 3.6\,(2.0) \cdot 10^{21}\ \text{Vm}^{-2}$ and $q^{\text{theor.}} = -1.86 \cdot 10^{21}\ \text{Vm}^{-2}$. Because of the small broadening of the Mössbauer resonance line the sign of q could not be determined experimentally.

The nitridoniccolate CaNiN contains infinite linear chains $^{1}_{\infty}[NiN_{2/2}]$ which run perpendicular to the c axis. Unexpectedly, $|q(\text{Ni})|$ in CaNiN is small: $q^{\text{exp.}} = 0.0\,(2.0) \cdot 10^{21}\ \text{Vm}^{-2}$ and $q^{\text{theor.}} = -3.05 \cdot 10^{21}\ \text{Vm}^{-2}$. Again the sign of q(Ni) could not be determined experimentally. It is found theoretically that the small value of q(Ni) is caused by severe cancellation between σ and π contributions.

1. Introduction

Chemical applications of ^{61}Ni Mössbauer spectroscopy are rare. The reason is that the experimental setup and the evaluation of the data is much more complicated than for ^{57}Fe. The short half life of the suitable parent nuclide ^{61}Co and a relatively high gamma energy of 67.4 keV require source activation near the Mössbauer spectrometer and measurements at low temperatures. Unfavourable nuclear parameters are the reason for usually poorly resolved spectra that require extensive fit procedures. Having overcome these hindrances, ^{61}Ni Mössbauer spectroscopy may provide very useful information about the studied systems.

To study the nickel-ligand bonds in more detail we have combined our experimental studies with theoretical investigations of the charge density distribution. Since it is possible to calculate the charge density sufficiently accurate within the self consistent band structure procedure, it is no longer necessary to use perturbation theory to get the electric field gradient (EFG) [1]. In the past ten years most of the band structure calculations were performed on the basis of the local density approximation which we also use. Here the linearized augmented plane wave (LAPW) and the APW methods give mostly excellent theoretical results [2–5]. However, for complicated structures with a large number of atoms per unit cell these methods can hardly be used because of computer limitations. Therefore, we use the faster full potential linear muffin-tin orbital (FP-LMTO) [6] method. For simple metals we have found that the EFG calculated by this method agrees quite well with the APW results. For example, for In metal the FP-LMTO result is $2.35 \cdot 10^{21}\ \text{Vm}^{-2}$ compared to the APW result of $2.67 \cdot 10^{21}\ \text{Vm}^{-2}$ and the experimental value $2.46 \cdot 10^{21}\ \text{Vm}^{-2}$ [5].

For our studies we have chosen the nickel compounds CaNiN, $BaNiO_2$ and $BaNiO_3$, which contain nickel in the formal oxidation states I, II and IV, re-

---

* Presented at the XIIIth International Symposium on Nuclear Quadrupole Interactions, Providence, Rhode Island, USA, July 23–28, 1995.

Reprint requests to Prof. Dr. P. C. Schmidt.

0932-0784 / 96 / 0500-0515 $ 06.00 © – Verlag der Zeitschrift für Naturforschung, D-72072 Tübingen

spectively. The crystal structure of CaNiN contains linear chains $^1_\infty[NiN_{2/2}]$, in $BaNiO_2$ nickel is in a planar coordination by four oxygen atoms and in $BaNiO_3$ nickel has an almost octahedral coordination sphere. In the following section we briefly outline some details of the ^{61}Ni Mössbauer experiments and the band structure calculation procedure. The resulting EFGs and charge density distributions for the compounds are given in Section 4.

2. Methods

2.1 ^{61}*Ni Mössbauer Experiments*

Sources of the parent ^{61}Co nucleus with $T_{1/2} =$ 99 min were produced at the MAinz MIcrotron (MAMI), which can provide an electron beam with up to 855 MeV energy and 100 μA current. A pneumatic tube was used to transport small platelets of $^{62}Ni_{0.85}Cr_{0.15}$ (97.7% enriched) alloy to the activation site in front of the beam dump of the three-spectrometer-setup of the A1 collaboration, allowing source activation during nuclear physics experiments. Bremsstrahlung including the giant resonance region of 20–25 MeV, necessary for the ^{62}Ni (γ, p) reaction, is produced from the electron beam directly in front of the activation area in a stack of air cooled gold foils. Immediately after activation, the sources are sealed in aluminium containers and transported to the Mössbauer setup.

A conventional vertical Mössbauer spectrometer in transmission geometry with a helium bath cryostat was used [7]. Samples were pressed into teflon sample holders by screwing one part into the other, while the thread was sealed with teflon tape. Source and absorber were in direct contact with liquid helium. The 67.4 keV radiation was detected with a 2 mm thick NaI (Tl) scintillator. For rapid installation, the source is pushed through a 1.47 m hollow stainless steel drive rod, which is moved with a sine velocity profile. To determine the effective thickness of the absorber, which is necessary for a correct calculation of the linewidth, pulse height spectra were recorded several times during the measurements to estimate the background radiation. On the other side of the transducer, ^{57}Fe Mössbauer spectra of α-iron could be run simultaneously allowing velocity calibration while recording ^{61}Ni spectra.

For the relevant nuclear levels with groundstate and excited spin states $I_g = \frac{3}{2}^-$ and $I_e = \frac{5}{2}^-$, respectively, a five component multiplet spectrum is observed for electric quadrupolar interaction in the absence of a magnetic field. In principle, the value, sign, and asymmetry parameter may be determined from this multiplet spectrum (for details see [8]).

Unfortunately the natural linewidth of the γ-transition is larger than the quadrupole interaction energy. However, the multiplet spectrum might show sufficient structure to determine the value and the sign of the largest component of the EFG, q. Values on the order of $q \sim 4 \cdot 10^{21}\ Vm^{-2}$ may be detected if "line broadening" by magnetic interaction can be excluded for the relevant component. Broadening by isomer shift can be excluded because of the small value of the difference of the nuclear charge radius.

Evaluation of the EFG parameters was performed with a new version [9] of the fit program MOSFUN [10] which, in addition to calculate the convolution integral, solves the spin hamiltonian for source and absorber, allowing to fit both relevant parameters q and asymmetry parameter η simultaneously.

The line broadening [11–13] of the $^{62}Ni_{0.85}Cr_{0.15}$ source was taken into account with a hyperfine magnetic field of 0.8 T known from earlier measurements and confirmed by evaluation of the single-line spectra of K_2NiF_6. The natural line width was calculated from the average of measurements of the life time of the exited state [14] to be $\Gamma_{nat} = 0.385\ mm\ s^{-1}$. The Lamb Mössbauer factor of the source ($f_{source} = 0.11$) was taken from [15].

2.2 *Band Structure Calculations*

The band structure calculations were performed by the scalar-relativistic full potential linear muffin-tin orbital (FP-LMTO) procedure [6]. We shall describe briefly those details of the method which are important for the investigation of the chemical bond and the EFG.

The standard LMTO procedure [16] is based on the atomic sphere approximation. The crystal potential "seen" by the electrons is approximated by a spherically symmetric potential inside overlapping spheres around the nuclei. This differs from the FP-LMTO method where the crystal potential has the correct symmetry of the lattice. Here the crystal volume is separated into two different regions. Region I are non-overlapping muffin-tin spheres around the nuclei, and region II is the interstitial region.

The electronic charge density $-e\varrho(\boldsymbol{r})$ of the crystal is calculated from the one-electron Bloch states $\psi_{\boldsymbol{k},n}(\boldsymbol{r})$,

$$\varrho(\boldsymbol{r}) = \sum_{\boldsymbol{k},n} |\psi_{\boldsymbol{k},n}(\boldsymbol{r})|^2, \tag{1}$$

where $\boldsymbol{k}$ is the wave vector and the n is the band index. The summation is taken over all occupied states. The $\psi_{\boldsymbol{k},n}(\boldsymbol{r})$ are expanded in basis functions ϕ_i which are constructed in almost the same way as is done for the LMTO-ASA method. A spherical Hankel function times a spherical harmonic is centered on some atom v in the unit cell. The Bloch sum of this object is called an envelope function and defines the basis function in the interstitial region. Inside all muffin-tin spheres, the envelope function is replaced by a smoothly-matching solution of Schrödinger's equation for the spheridized potential inside the sphere. The full potential is used in all regions when setting up the secular matrices. Since Hankel functions of different localizations $\exp(-\kappa_\alpha)$ are used ("multiple kappa basis"), the index i stands for

$$i = (\boldsymbol{k}, v, l, m_l, \alpha)\,. \tag{2}$$

Then $\psi_{\boldsymbol{k},n}(\boldsymbol{r})$ is a linear combination of the basis functions,

$$\psi_{\boldsymbol{k},n}(\boldsymbol{r}) = \sum_i c_{i,n}\,\phi_i(\boldsymbol{r})\,. \tag{3}$$

The wave functions $\psi_{\boldsymbol{k},n}(\boldsymbol{r})$ are normalized over the unit cell

$$\int_{\text{unit cell}} |\psi_{\boldsymbol{k},n}(\boldsymbol{r})|^2\,\mathrm{d}\tau = 1\,. \tag{4}$$

According to the form of the basis functions, the integral over the unit cell and therefore also the density of states $N(E)$ can be split into l, m_l and v dependent contributions. That is, $N(E)$ can be separated into partial densities of states $N_{v,l,m_l}(E)$, describing the contribution of the muffin-tin spheres and the contribution of the interstitial region II, $N^{(\mathrm{MT})}_{\mathrm{out}}$,

$$N^{(\mathrm{MT})}(E) = \sum_{v}^{\text{unit cell}} \sum_{l} \sum_{m_l=-l}^{l} N^{(\mathrm{MT})}_{v,l,m_l}(E) + N^{(\mathrm{MT})}_{\mathrm{out}}\,. \tag{5}$$

Partial densities of states can also be defined in the sense of Mulliken charges. These partial densities of states are calculated from the projections

$$b_i = \langle\phi_i|\psi_{\boldsymbol{k},n}\rangle = \sum_j c_j\langle\phi_i|\phi_j\rangle\,. \tag{6}$$

For the compounds investigated here the shapes of the two types of partial densities of states, Mulliken or muffin-tin contributions, are similar and therefore give the same picture of the chemical bond in these compounds. In the following only the $N^{(\mathrm{MT})}_{v,l,m_l}(E)$ are displayed. For our investigations the partial m_l dependent densities of states are transformed into suitable cartesian coordinate systems (x, y, z) in order to discuss the chemical bonding mechanisms in terms of the atomic orbital picture.

Finally we want to give the expressions for the EFG within the FP-LMTO method. Usually in NQR the second derivative of the electrostatic potential $V(\boldsymbol{r})$ at the nuclear site $\boldsymbol{r} = 0$

$$V_{ij} = \left.\frac{\partial^2 V(\boldsymbol{r})}{\partial x_i\,\partial x_j}\right|_{\boldsymbol{r}=0};\; x_i = (x, y, z) \tag{7}$$

is called EFG (although the EFG is the negative of V_{ij}). To evaluate V_{ij} we can take advantage of the fact that the FP-LMTO charge density as well as the electrostatic potential are expanded in spherical harmonics Y_{l,m_l} around the nuclear positions. Then we can write

$$\varrho(\boldsymbol{r}) = \sum_{l,m_l} \varrho_{l,m_l}(r)\,Y_{l,m_l}(\hat{r}) \tag{8}$$

and

$$V(\boldsymbol{r}) = \sum_{l,m_l} V_{l,m_l}(r)\,Y_{l,m_l}(\hat{r})\,. \tag{9}$$

Taking the second derivative of (9) at $\boldsymbol{r} = 0$, only the components for $l = 2$ are non-vanishing. One obtains

$$V_{ij} = \sum_{m_l=-2}^{2} C^{m_l}_{i,j}\,A_{2,m_l}, \tag{10}$$

where the A_{2,m_l} are the leading terms of the radial potential functions

$$A_{2,m_l} = \lim_{r\to 0}\frac{V_{2,m_l}(r)}{r^l}, \tag{11}$$

and the coefficients $C^{m_l}_{i,j}$ are given by

$$C^{m_l}_{i,j} = \left.\frac{\partial^2 (r^l\,Y_{2,m_l}(\hat{r}))}{\partial x_i\,\partial x_j}\right|_{\boldsymbol{r}=0}, \tag{12}$$

e.g. $C^0_{zz} = \sqrt{\frac{5}{\pi}}$ and $V_{zz} = A_{2,0}(0)\sqrt{\frac{5}{\pi}}$.

Within the FP-LMTO method, the Poisson equation is solved as follows. The Poisson equation is first solved inside each muffin-tin (MT) sphere (with radius R) using the von Neumann boundary conditions $V(\boldsymbol{R}) = 0$, giving a potential $V^{(\mathrm{P})}(\boldsymbol{r})$. As in [17], a pseudodensity is made which equals the true density in the interstitial and has the correct multipole moments

$$q_{l,m_l} = \int_{\mathrm{MT}} Y_{l,m_l}(\hat{r})\,r^l\,\varrho(\boldsymbol{r})\,\mathrm{d}\tau \tag{13}$$

inside the MT spheres. The interstitial density is given as a sum of atom-centered Hankel functions, so the pseudodensity equals this expression extended into the MT spheres plus point multipoles which correct the moments. The Poisson equation is solved analytically for the pseudodensity, giving the correct potential in the interstitial and the values of the potential on each MT sphere. To match the sphere potential from the first step to these values, the following solution of the Laplace equation inside the sphere is added:

$$V^{(L)}(\boldsymbol{r}) = \sum_{l,m_l} w_{l,m_l} \frac{r^l}{R^l} Y_{l,m_l}(\hat{r}), \qquad (14)$$

where the coefficients w_L give the potential on the sphere surface ($r = R$).

An angular momentum component of the electrostatic potential near the nucleus is thus given by the sum $V_{l,m_l}(r) = V^{(P)}(r) + V^{(L)}(r)$. The leading terms A_{l,m_l} and the field gradient decompose into corresponding contributions, i.e.,

$$A_{l,m_l} = A^{(P)}_{l,m_l} + A^{(L)}_{l,m_l} \qquad (15)$$

(where $A^{(L)}_{l,m_l}$ is simply $w_{l,m_l}/R^l$).

We note that a different decomposition of the field gradient into a MT and an external part is sometimes used. A MT contribution can be defined using the potential due to the charge density inside the MT sphere according to Coulomb's law,

$$V^{(MT)} = \frac{-e}{4\pi\varepsilon_0} \int_{MT} \frac{\varrho(\boldsymbol{r}')\,d\tau'}{|\boldsymbol{r} - \boldsymbol{r}'|}, \qquad (16)$$

which has the leading terms

$$A^{(MT)}_{l,m_l} = \frac{-e}{4\pi\varepsilon_0} \int_0^R \frac{\varrho_{l,m_l}(r)}{r^3} r^2\,dr. \qquad (17)$$

The potentials $V^{(MT)}$ and $V^{(P)}$ used in the FP-LMTO method are related by

$$V^{(MT)}_{l,m_l}(r) = V^{(P)}_{l,m_l}(r) + \frac{4\pi q_{l,m_l}}{(2l+1)R^{2l+1}} r^l. \qquad (18)$$

Thus, the leading term $A^{(MT)}_{l,m_l}$ is

$$A^{(MT)}_{l,m_l} = A^{(P)}_{l,m_l} + \frac{4\pi q_{l,m_l}}{(2l+1)R^{2l+1}}. \qquad (19)$$

In the following the EFG tensor is always transformed to its principal axes system (x', y', z'). That is,

$$q = V_{z'z'}$$

and the asymmetry parameter is

$$\eta = \frac{V_{x'x'} - V_{y'y'}}{V_{z'z'}}.$$

In order to obtain reasonable theoretical results for the EFG for the compounds investigated here a triple kappa basis set has to be used. The expansions in spherical harmonics are up to $l_{\max,b} = 3$ for the head of the basis functions, up to $l_{\max,a} = 4$ for the tails of the basis functions in the MT-spheres and up to $l_{\max,f} = 5$ for the expansion of the interstitial potential and charge density.

3. Crystal Structures and Sample Preparation

CaNiN [18] (see Fig. 1) is an isotype of the YCoC type structure [19] and also isotype to SrLiN [20]. The crystal structure is tetragonal (Space group $P4_2/mmc$, $a = 358.09(2)$ pm, $c = 700.96(3)$ pm), the atomic positions are Ca at $2e$ (0, 0, 0.25), Ni at $2b$ (0.5, 0.5, 0), and N at $2c$ (0, 0.5, 0). Nickel is in a linear coordination by nitrogen. The $\overset{1}{\infty}[NiN_{2/2}]$ chains are arranged in layers perpendicular to the c-axis. Adjacent layers along [001] are stacked by turning by 90°. Calcium is situated between the layers and is in a tetrahedral coordination by nitrogen.

In the crystal structure of $BaNiO_2$ [21–23] (Fig. 2) nickel is in a square-planar coordination by oxygen. (Space group $Cmcm$, $a = 573.5(5)$ pm, $b = 919{,}0(5)$ pm, $c = 475.5(5)$ pm, atomic positions: Ba at $4c$ (0, 0.345, 0.25), Ni at $4a$ (0, 0, 0) and O at $8g$ (0.25, 0.080, 0.25)

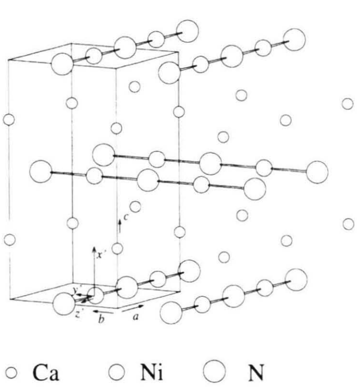

Fig. 1. Crystal structure of CaNiN. (x', y', z') is the principal axes system of the calculated EFG at the nickel site. This axes system is equal to the axes system used for the representation of the partial m_l dependent densities of states (x, y, z).

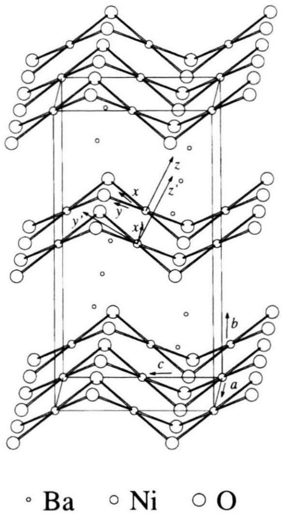

Fig. 2. Crystal structure of $BaNiO_2$. (x', y', z') is the principal axes system of the calculated EFG at the nickel site. The axes system (x, y, z) is used for the representation of the partial m_l dependent densities of states.

[22].) The nickel-oxygen squares share opposite edges and form puckered chains which run along the crystallographic c-axis. Barium is eight-fold coordinated by oxygen and occupies positions between the layers of the $NiO_{4/2}$ chains.

$BaNiO_3$ [21–24] contains nickel in a distorted octahedral coordination. The crystal structure of hexagonal $BaNiO_3$ can be derived from the $BaNiO_2$ structure by adding oxygen atoms, above and below the square planes resulting in face-sharing chains of NiO_6 octahedra running along the c-axis (see Figure 3). The structure can be described in terms of a 2H hexagonal variant of the cubic perovskite structure [23]. Barium is in a twelve-fold coordination by oxygen. The crystallographic data are as follows: space group: $P6_3/mmc$, $a = 562.9(3)$ pm, $c = 481.1(3)$ pm, Ba at $2d$ (1/3, 2/3, 3/4), Ni at $2a$ (0, 0, 0), O at $6h$ (0.1462, −0.1462, 0.25) [24].

CaNiN was prepared by heating calcium and nickel in an alumina crucible under nitrogen at 1000 °C for 10 h. The samples were examined by X-ray powder diffraction and atomic absorption spectroscopy. They contained small amounts of metallic nickel as well as Ca_3N_2. Excess calcium (10 to 20%) was used during the preparation in order to reduce the nickel impurities. The nickel impurities did not impair the evaluation of the Mössbauer spectra. $BaNiO_2$ was obtained by a reaction of NiO and $BaCO_3$ at 1100 °C under vaccum. $BaNiO_2$ was heated under oxygen atmosphere at 560 °C to obtain $BaNiO_3$. The iodometric determination of the oxygen content of $BaNiO_3$ gave the exact stoichiometry $BaNiO_{2.94}$. From magnetic susceptibility measurements both $BaNiO_{2.94}$ and $BaNiO_2$ samples are diamagnetic. A weak paramagnetic contribution is due to impurities.

4. Results and Discussion

4.1 $BaNiO_3$

The Mössbauer spectrum of $BaNiO_3$ is shown in Figure 4. The intensity of the slightly broadened line corresponds to an absorber thickness of $t_{\mathrm{eff}} = 0.78(5)$ from which a Lamb-Mössbauer factor of 0.11(1) can be deduced. From magnetic susceptibility measurements it is known that $BaNiO_3$ is diamagnetic [22], and therefore the unresolved splitting must be caused by a quadrupole splitting equivalent to an EFG $q = \pm 3.6(2.0) \cdot 10^{21}$ Vm^{-2}. With the given statistics, the relatively small splitting did neither allow the determination of the sign of q nor of η.

In the crystal field model, the electronic contributions to q cancel out for a d^6-system in the low spin state with octahedral coordination because only the d_{xy}, d_{yz}, and d_{xz} orbitals are occupied [21–23]. Therefore, a small value of q for $BaNiO_3$ is understandable due to the slight octahedral distortion and a nonvanishing lattice contribution.

For our band structure calculations we introduced empty spheres E at positions $6h$ (0.41, 0.82, 0.25).

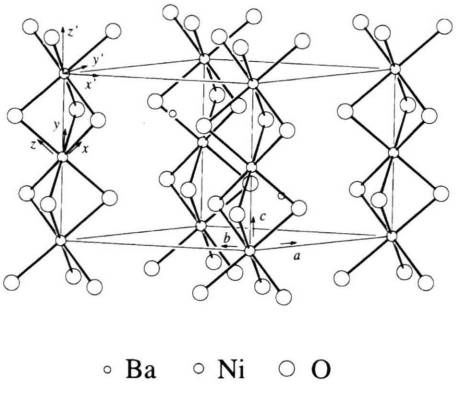

Fig. 3. Crystal structure of $BaNiO_3$. (x', y', z') is the principal axes system of the calculated EFG at the nickel site. The axes system (x, y, z) is used for the representation of the partial m_l dependent densities of states.

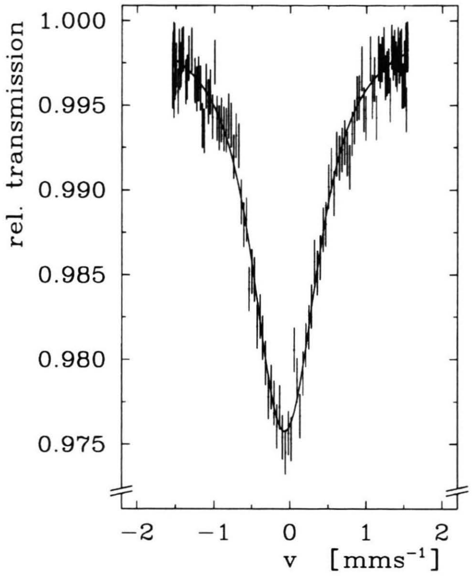

Fig. 4. ^{61}Ni Mössbauer spectrum of $BaNiO_3$.

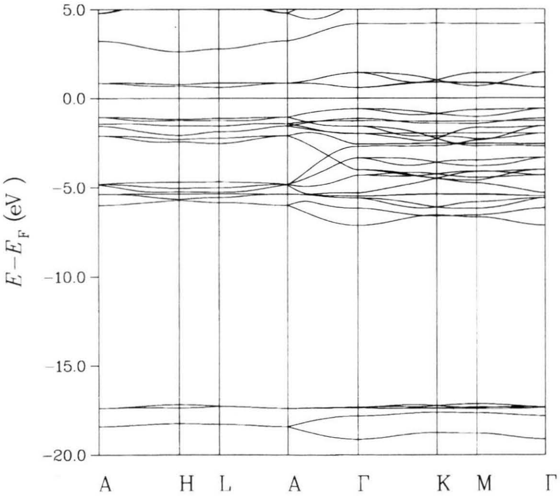

Fig. 5. Band structure of $BaNiO_3$.

The muffin-tin radii are $R_{Ba} = 185.2$ pm ($3.5\ a_0$), $R_{Ni} = 84.7$ pm ($1.6\ a_0$), $R_O = 84.7$ pm ($1.6\ a_0$) and $R_E = 63.5$ pm ($1.2\ a_0$). We used 297 $\boldsymbol{k}$-points in the irreducible part of the Brillouin zone. From our theoretical studies the principal axes system of V_{ij}(Ni) shown in Fig. 3 results. For q(Ni) we obtain $-1.86 \cdot 10^{21}$ Vm^{-2}, η is zero because of the point symmetry.

Details of the bonding in $BaNiO_3$ are shown in Figs. 5, 6, and 7, where the band structure, the partial density of states and contour plots of the valence charge density are displayed. The lowest bands shown in Fig. 5 are the $2s$(O) like bands which do not contribute to the chemical bond. Above these states up to the Fermi energy we find the oxygen-nickel bonds. We find a band gap at the Fermi level. As the density functional approach usually underestimates the band gap, we expect that the experimental optical band gap should be larger than the one shown in Figure 5.

The bonding mechanism can be seen in more detail in Figs. 6 and 7. First we look at the bonding of barium. We see from the partial densities of states in Fig. 6 that the contributions $N_{Ba,l}(E)$ are small for the energy range below E_F. These small contributions result predominantly from the tails of the basis functions. Therefore, barium is ionic. This can also be seen from the contour lines of the (100) ($x = 0$) plane in Figure 7: There is a distinct deficit of charge in the region of the Ba atoms.

In the same plane we also see the strong covalent bonds between nickel and oxygen. These are the states between -7.6 and -1.1 eV in Figure 6. The bonds result in common peaks of the d(Ni) and p(O) partial densities of states. This FP-LMTO band structure result differs from a CNDO calculation where the p(O) states are lying above the d(Ni) states separated by a band gap [25]. The same holds for $BaNiO_2$, see below.

In order to compare the band structure results with the crystal field theory, the partial densities of states are transformed into the axes system of the NiO_6 octahedron which is usually used in crystal field theory. As the octahedron has a trigonal distortion, the axes system does not fit exactly to the nickel-oxygen directions. The occupation of the electronic states differs from the one in the pure crystal field picture. The lowest states at -6 eV are bonding Ni-O states described by the overlap of the $(d_{x^2-y^2}, d_{z^2})$(Ni) and p(O) orbitals. The corresponding antibonding states are above E_F. Between these states we find the almost non-bonding d_{xy}(Ni), d_{yz}(Ni) and d_{xz}(Ni) states. The d_{xy}(Ni), d_{yz}(Ni) and d_{xz}(Ni) states as well as the d_{z^2}(Ni) and $d_{x^2-y^2}$(Ni) states are nearly degenerate and correspond to the t_{2g} and e_g atomic orbitals in an octahedral crystal field.

The contour lines for the planes (100) and (120) in Fig. 7 show the Ni-Ni bonds along the c axis caused by an overlap of d(Ni) orbitals. Chosing an axes sys-

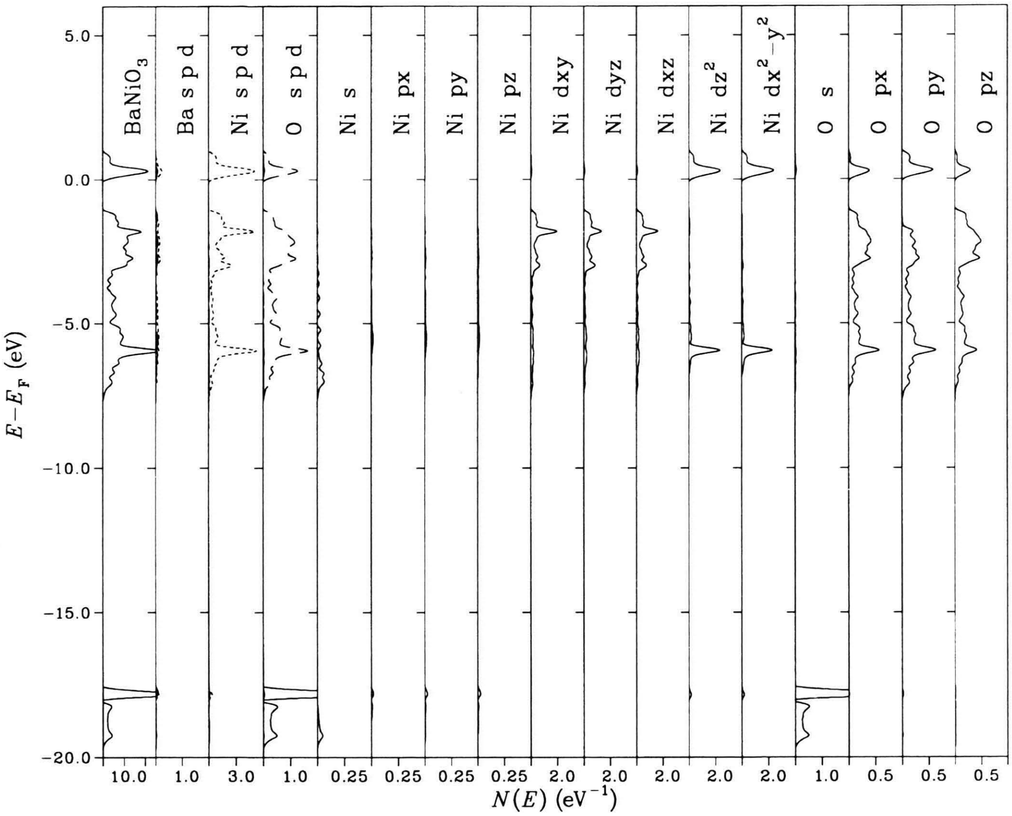

Fig. 6. Total and partial densities of states of $BaNiO_3$. In panels 2–4 the *s*, *p* and *d* contributions are plotted as solid, dashed and dotted curves. The axes system (*x*, *y*, *z*) is shown in Figure 3.

tem in which the *z* axis runs along the crystallographic *c* axis, the distinct maximum in $N(E)$ at -1.8 eV belongs to $N_{\mathrm{Ni},d_{z^2}}$. From the contour lines in the (001) plane we see the six fold axis and only weak contacts between the Ni atoms within this plane. The negative sign of q can be understood qualitatively from the prolate shape of the charge density around the Ni nuclei which can be seen from the contour lines in the (120) plane in Figure 7. However, it should be pointed out that a prolate charge density outside the core region of the corresponding atoms does not always indicate a negative EFG.

4.2 $BaNiO_2$

$BaNiO_2$ also was found to be diamagnetic [21–23], therefore no magnetic hyperfine splitting was expected. Figure 8 shows the ^{61}Ni Mössbauer spectrum of $BaNiO_2$. The effect corresponds to an absorber thickness of $t_{\mathrm{eff}} = 1.4(2)$ ($f_{\mathrm{abs}} = 0.22(3)$). The large asymmetric splitting in the Mössbauer spectrum must be entirely caused by the nuclear quadrupole interaction. From the shape of the spectrum one derives $q^{\mathrm{exp.}} = -15.7(1.5) \cdot 10^{21}$ Vm^{-2}, which is one of the largest values ever found by ^{61}Ni Mössbauer spectroscopy, while η was found to be smaller than 0.4. The large size of the EFG is expected because of the square-planar coordination of nickel by oxygen. In the low spin state the crystal field theory predicts a hole in the b_{1g} level ($d_{x^2-y^2}$ orbital), strongly reducing positive contributions to q. This is known as the textbook [8] example for strong quadrupole splitting. Therefore, the principal *z* axis should be perpendicular to the NO_4 square. This is also found by the band structure calculation. The calculated principal axes system is shown in Figure 2. Using our theory we calculate a large negative q value of $-15.59 \cdot 10^{21}$ Vm^{-2}, and η is equal to 0.33. These

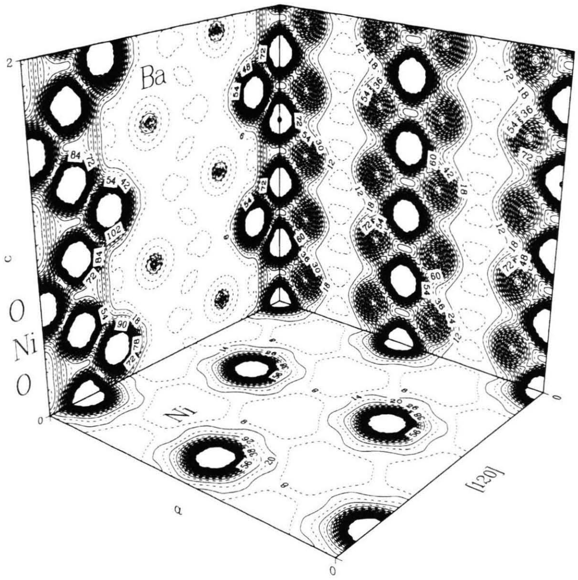

Fig. 7. Contour plots of the valence charge density of $BaNiO_3$. The selected planes are (001) ($c = 0$, $z' = 0$), (100) ($a = 0$, $x' = 0$) and (120) ($y' = 0$). The charge density is given in multiples of 10^{-3} $(-e)/a_0^3$ ($a_0 = 52.918$ pm). (x', y', z') are the principal axes of the EFG at the nickel site.

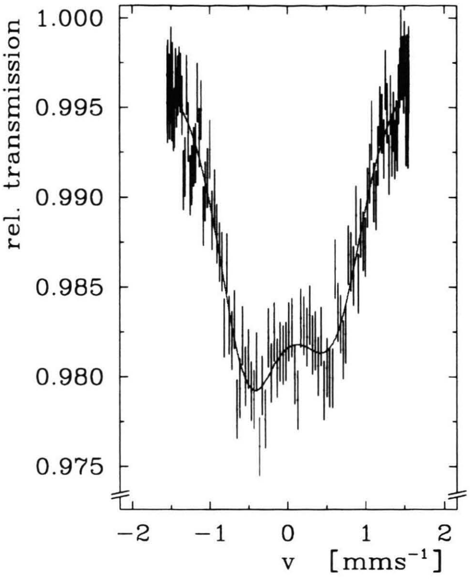

Fig. 8. ^{61}Ni Mössbauer spectrum of $BaNiO_2$.

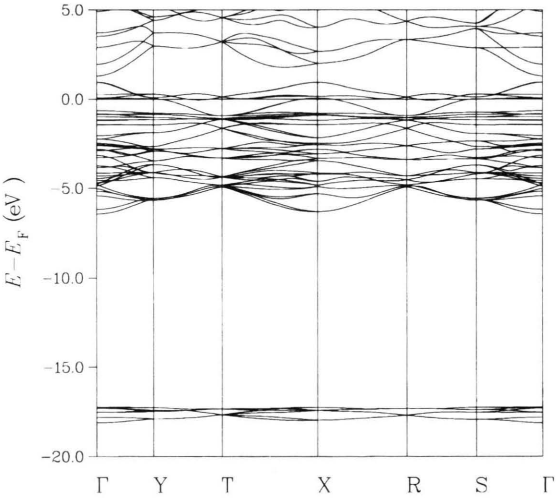

Fig. 9. Band structure of $BaNiO_2$.

findings are in agreement with the experimental results.

For the calculations, empty spheres E at 4*c* (0.5, 0.7, 0.75) are introduced. The muffin-tin radii for $BaNiO_2$ are chosen as $R_{Ba} = 169.3$ pm ($3.2\ a_0$), $R_{Ni} = 111.1$ pm ($2.1\ a_0$), $R_O = 84.1$ pm ($1.59\ a_0$) and $R_E = 79.4$ pm ($1.5\ a_0$). The total number of used $\boldsymbol{k}$-points in the irreducible part of the Brillouin zone is 216. The band structure results for $BaNiO_2$ are summarized in Figs. 9, 10 and 11. As in $BaNiO_3$, the bonding between barium and the nickel-oxygen chains is almost ionic and we find strong covalent oxygen-nickel bonds. However, in contrast to $BaNiO_3$ we do not find a band gap at the Fermi level. It might be that this finding is caused by the approximation for the exchange-correlation potential which also predicts no optical band gap for NiO. For NiO it is demonstrated that this incorrect result can be traced back to the approximate correlation potential and the self energy term [26]. Nevertheless it should be mentioned that the electrical resistivity of $BaNiO_2$ is by a factor of 2000 smaller than that of $BaNiO_3$ [22].

The details of the nickel oxygen bonds can be seen from the m_l-dependent partial density of states displayed in Figure 10. In the chosen axes system the x and y axes run along the nickel oxygen bonds. The lowest states between -6 and -4 eV are p(O)-$d_{x^2-y^2}$(Ni) bonds. Between -4 and -2 eV we find electronic states which have a slight admixture of d(Ni) components. Above these states up to E_F we find the d_{xy}, d_{yz}, d_{yz}, and d_{z^2} states which are the predicted occupied orbitals in the crystal field theory. However, also for these states we find a covalent bonding contri-

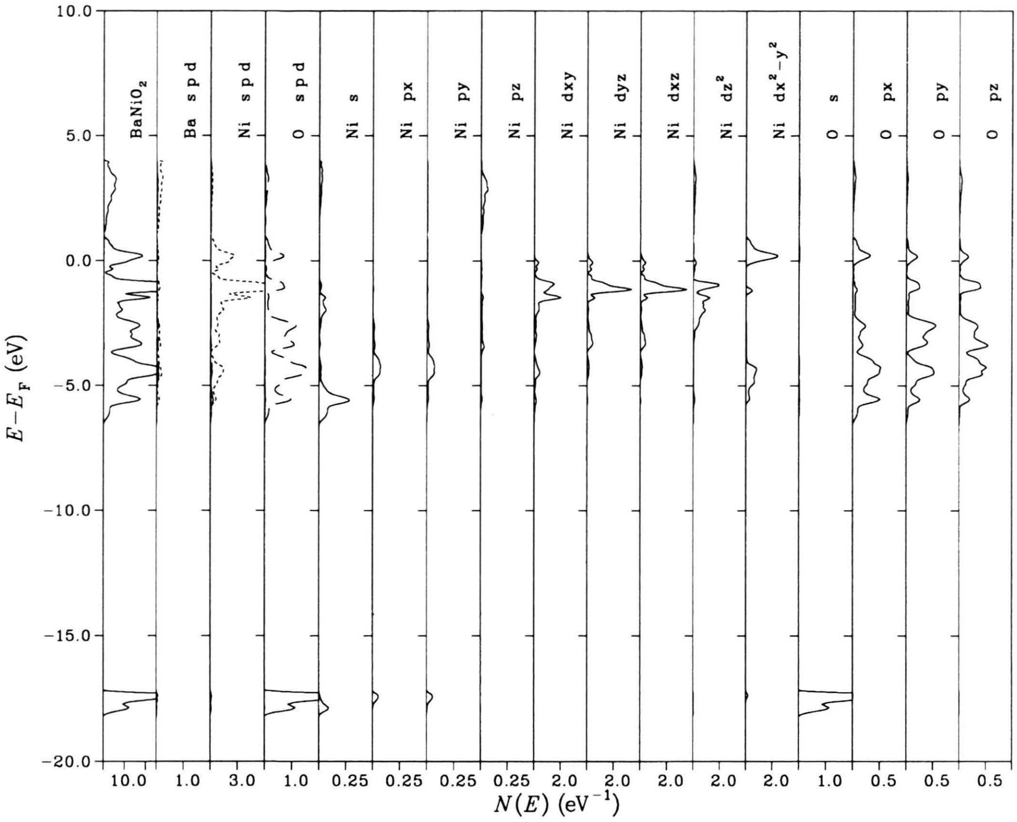

Fig. 10. Total and partial densities of states of $BaNiO_2$. In panels 2–4 the *s*, *p* and *d* contributions are plotted as solid, dashed and dotted curves. The axes system (*x*, *y*, *z*) is shown in Figure 2.

bution. Considering the nuclear quadrupole interaction, both models, the crystal field theory and the band structure approach predict a deficit in the occupation of the $d_{x^2-y^2}$ like states which causes a large negative EFG.

4.3 CaNiN

Figure 12 shows the ^{61}Ni Mössbauer spectrum of CaNiN. The sample contained impurities of nickel metal and Ca_3N_2. Thus, the spectrum consists of two components which may be easily separated by the fitting procedure. Nickel metal is known to be split by a magnetic hyperfine field of 7 T forming almost a quartet, the single line with a broadening within the error must therefore be assigned to CaNiN. Knowing the overall nickel content and the parameters for Ni metal [27], the *f*-factor could be determined. From the effective thickness (Ni metal: 0.7(1), CaNiN: 1.1(1)) the Lamb-Mössbauer factor of CaNiN was calculated to be $f_{\text{abs}} = 0.13(2)$. For $q^{\text{exp.}}$ we calculate a value of $0.0(2.0) \cdot 10^{21}\ \text{Vm}^{-2}$. From magnetic susceptibility measurements [18] a change from paramagnetic to antiferromagnetic behavior at 7 K was concluded. The lack of a magnetic hyperfine field in the Mössbauer spectrum of CaNiN may be explained by rapid fluctuations of the spin orientation, too fast for the Mössbauer time window. The small linewidth also excludes a larger value of q that might have been expected from a linear coordination of a d^9 or $d^8\,s^1$ ion in terms of a crystal field approach. In this picture, a hole in the a_{1g} level (d_{z^2} orbital) should result in a substantial positive q value. The failure of this simple approach is caused by the covalent bonding in this compound, which shall be explained next.

For the band structure calculations of CaNiN empty spheres E are positioned at 2*d* (0.5, 0, 0). The muffin-tin radii are $R_{\text{Ca}} = 177.3$ pm ($3.35\,a_0$), $R_{\text{Ni}} = 115.4$ pm

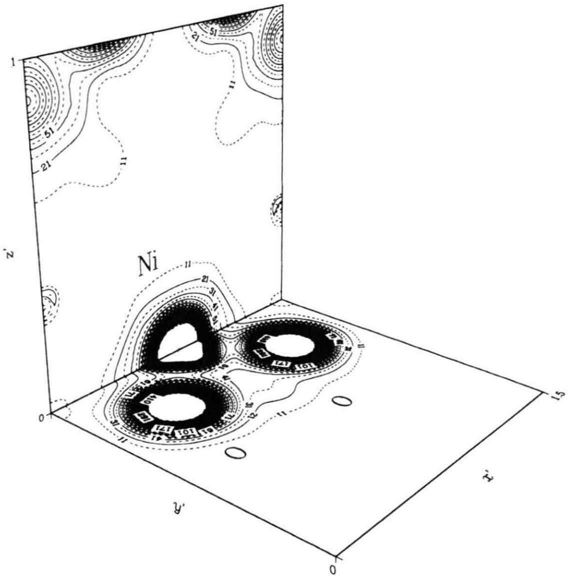

Fig. 11. Contour plots of the valence charge density of $BaNiO_2$. The selected planes are ($y' = 0$) and ($z' = 0$). The charge density is given in multiples of $10^{-3}\,(-e)/a_0^3$ ($a_0 = 52.918$ pm). (x', y', z') are the principal axes of the EFG at the nickel site.

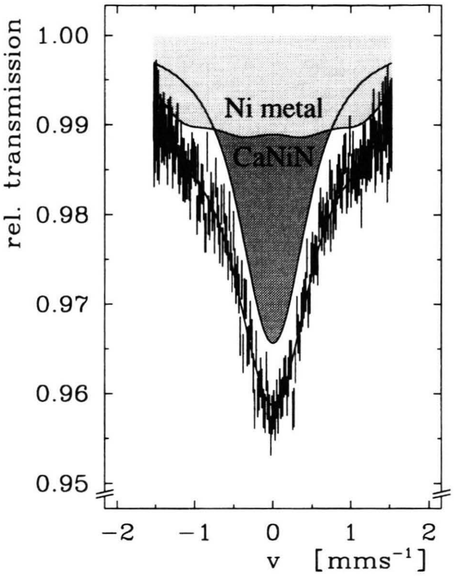

Fig. 12. ^{61}Ni Mössbauer spectrum of CaNiN.

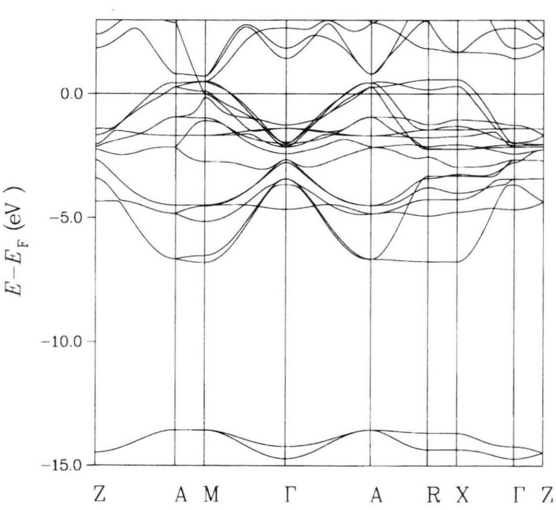

Fig. 13. Band structure of CaNiN.

($2.18\,a_0$), $R_N = 63.5$ pm ($1.2\,a_0$) and $R_E = 63.5$ pm ($1.2\,a_0$). The calculations were performed for 288 $\boldsymbol{k}$-points in the Brillouin zone. In Figs. 13, 14, and 15 we show the electronic states of CaNiN. The band structure is in agreement with the results from a LAPW calculation of Massidda et al. [28]. The lowest valence bands are the non bonding N $2s$ like states. The alkaline earth metal is almost ionic, and the width of the bands which are formed by the nickel-nitrogen bonding and antibonding states is the same as the bands of the nickel oxygen states shown in Figs. 6 and 10. The contour lines in the (001) ($c = 0$) and (010) ($b = 0.25$) plane in Fig. 15 show the strong Ni-N bonds in the nickel nitrogen chains. The bonds between the chains are distinctly weaker.

From the m_l dependent partial densities of states we can see the σ and π character of the nickel-nitrogen bonds. Between -7 and -5 eV are the s(Ni)-p_z(N) σ bonds; in the range -5 to -3 eV we find the $\sigma\, p_z$(Ni)-p_z(N) bonds and the d_{xz}, d_{yz}(Ni)-p_x, p_y(N) π bonds. The π bonds extend up to the Fermi energy. The d_{xy}(Ni) partial density of states give a relatively narrow peak, indicating localized nonbonding states. In the case of an isolated infinite Ni-N chain no molecular orbital of p(N) and d_{xy}(Ni) functions is possible because of the δ symmetry of the d_{xy} orbital. The $d_{x^2-y^2}$(Ni) states are broader than the d_{xy}(Ni) states, which can be explained by a weak Ni-Ni bonding between neighbored chains in y direction (see also Figure 1).

The calculated EFG is $q^{\text{teor.}} = -3.05 \cdot 10^{21}$ Vm^{-2}, which is in reasonable agreement with the experimental finding. The theoretical value for η is 0.445. Analyzing the various contributions to the EFG we

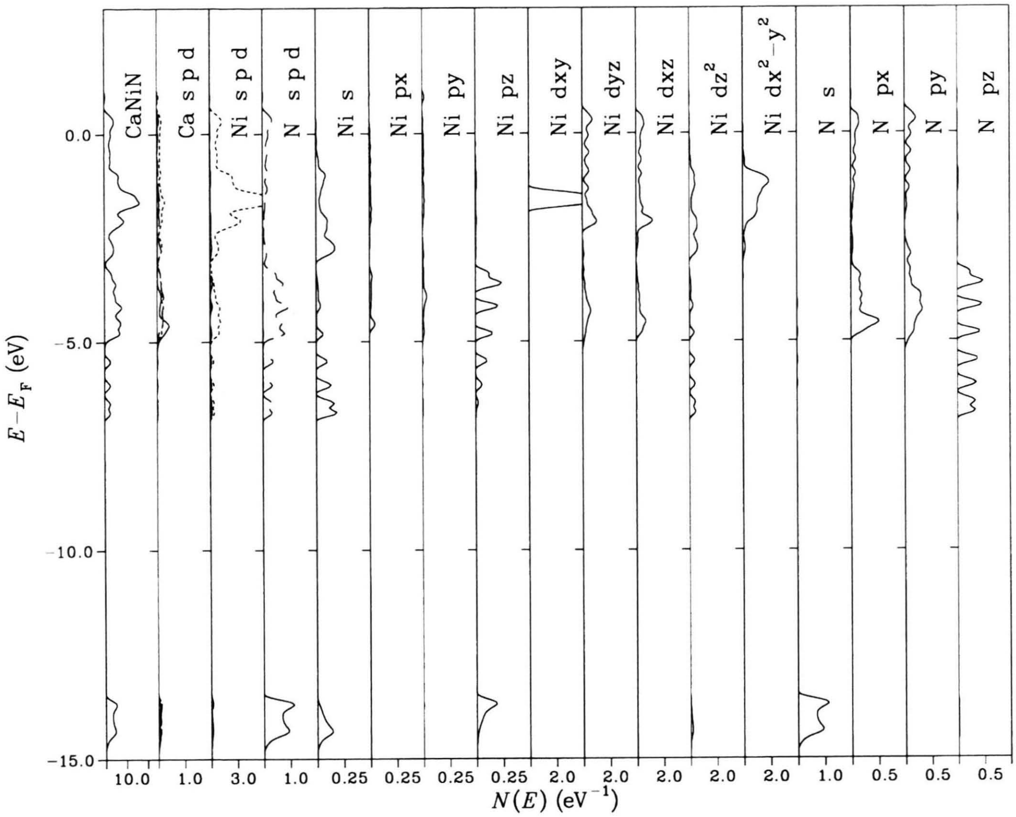

Fig. 14. Total and partial densities of states of CaNiN. In panels 2–4 the *s*, *p* and *d* contributions are plotted as solid, dashed and dotted curves. The axes system (*x*, *y*, *z*) is shown in Figure 1.

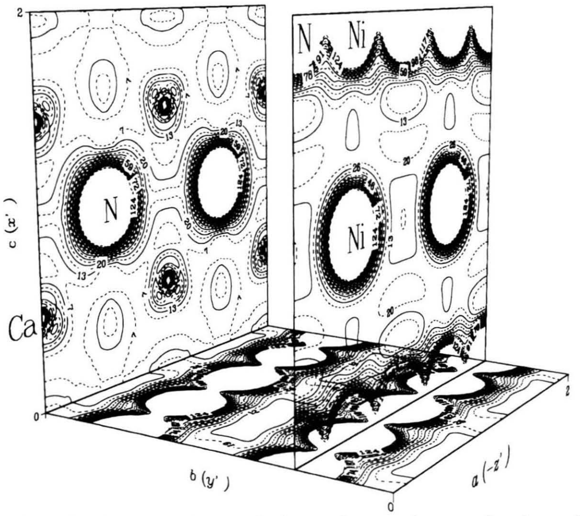

Fig. 15. Contour plots of the valence charge density of CaNiN. The selected planes are (001) ($c = 0$), (010) ($b = 0$) and (010) ($b = 0.25$). The charge density is given in multiples of $10^{-3}\,(-e)/a_0^3$ ($a_0 = 52.918$ pm). (x', y', z') are the principal axes of the EFG at the nickel site.

find large contributions from the π and σ bonds, which have different signs and almost cancel each other. This can be seen by calculating $V_{20}^{(\mathrm{MT})}(0)$ from (16) for different energy ranges. For the σ states in the energy range of up to -5.1 eV the q contribution is $-26.02 \cdot 10^{21}$ Vm^{-2}. For the range from -5.1 to -3.1 eV, where we have a mixture of σ and π bonds, we derive $-39.34 \cdot 10^{21}$ Vm^{-2} and for the -3.1 to 0 eV energy range the almost pure π contribution is $62.52 \cdot 10^{21}$ Vm^{-2}.

5. Conclusion

For the three nickel compounds CaNiN, BaNiO$_2$ and BaNiO$_3$, which contain nickel in three different oxidation states (I, II, and IV, resp.) we have studied the electric field gradient at the nickel site by ^{61}Ni Mössbauer spectroscopy and by the full potential linear muffin tin orbital band structure procedure. The quantitative agreement between both methods is very satisfactory, and from the combination of the experimental and theoretical methods one can explain the quadrupole hyperfine interaction from the analysis of the bonding mechanism. It is found that, besides the crystal field splitting in the ionic model, the covalent nickel-ligand bonds play an important role in the interpretation of the nuclear quadrupole interaction.

Acknowledgements

We thank the Institut für Kernphysik at the University of Mainz for the possibility of and support in source activation. This work was supported by the Deutsche Forschungsgemeinschaft, the Fonds der Chemischen Industrie and the Materialwissenschaftliches Forschungszentrum der Universität Mainz.

[1] R. M. Sternheimer, Z. Naturforsch. **41a**, 24 (1986).
[2] P. Blaha, K. Schwarz, and P. Herzig, Phys. Rev. Lett. **54,** 1192 (1985).
[3] P. Blaha, K. Schwarz, and P. H. Dederichs, Phys. Rev. B **37** (6), 2792 (1988).
[4] K. Schwarz and P. Blaha, Z. Naturforsch. **47a,** 197 (1991).
[5] R. Leiberich, P. C. Schmidt, N. Sahoo, and T. P. Das, Z. Naturforsch. **45a,** 368 (1990).
[6] M. Methfessel, Phys. Rev. B **38**(2), 1537 (1988).
[7] K. Römhild, PhD Thesis, Mainz 1982.
[8] P. Gütlich, R. Link, and A. Trautwein, Inorganic Chemistry Concepts, volume 3. Springer-Verlag, Berlin 1978.
[9] H. Spiering, private communication 1995.
[10] E.-W. Müller, Mössbauer Effect Reference and Data Journal **4,** 89 (1981).
[11] U. Erich, Z. Physik **227,** 25 (1969).
[12] H. Rummel, PhD Thesis, Mainz 1982.
[13] P. Griesbach, private communication.
[14] H. Visser, S. Roodbergen, W. Molendijk, H. S. Bedet, and H. Verheul, Z. Physik A **275,** 45 (1975).
[15] W. Krug, Darmstadt, quoted from [12].
[16] O. K. Anderson, Phys. Rev. B **12** (8), 3060 (1975).
[17] M. Weinert, J. Math. Phys. **22** (11), 2433 (1981).
[18] M. Y. Chern and F. J. DiSalvo, J. Solid State Chem. **88,** 459 (1990).
[19] M. H. Gerss and W. Jeitschko, Z. Naturforsch. **41b,** 946 (1986).
[20] G. Cordier, A. Gudat, R. Kniep, and A. Rabenau, Angew. Chem. **101** (2), 204 (1989).
[21] J. J. Lander, Acta Cryst. **4,** 148 (1951).
[22] H. Krischner, K. Torkar, and B. O. Kolbesen, J. Solid State Chem. **3,** 349 (1971).
[23] J. DiCarlo, I. Yazdi, A. J. Jacobson, and A. Navrotsky, J. Solid State Chem. **109,** 223 (1994).
[24] Y. Takeda, F. Kanamaru, M. Shimada, and M. Koizumi, Acta Cryst. **B32,** 2464 (1976).
[25] R. A. Evarestov, V. A. Veryazov, I. I. Tupitsyn, and V. V. Afanasiev, J. Electron Spectrosc. Relat. Phenom. **68,** 555 (1994).
[26] A. Svane and O. Gunnarson, Phys. Rev. Lett. **65** (9), 1148 (1990).
[27] J. C. Love, F. E. Obenshain, and G. Czjzek, Phys. Rev. **B3,** 2827 (1971).
[28] S. Massidda, W. E. Pickett, and M. Posternak, Phys. Rev. B **44** (3), 1258 (1991).